## PAPER

Check for updates

# Synergistic absorbents based on SnFe₂O₄@ZnO nanoparticles decorated with reduced graphene oxide for highly efficient dye adsorption at room temperature†

Pawan Kumar Singh,[a] Kuan-Yi Kuo,[a] Jui-Teng Lee,[a] Po-Hsuan Hsiao,[a] Joon Ching Juan, [ID] [b] Hong Phan Duong [ID] [c] and Chia-Yun Chen [ID] ⋆[ad]

Recently, adsorption techniques have emerged as practical and effective methods for removing organic dyes, dramatically extending practical capabilities for treating deleterious pollutants in wastewater. However, an urgent issue restricting the performance of these techniques is that no available absorbents that can be used to treat both cationic and anionic organic dyes have been made with simple and reliable methods until now. Herein, we report a green synthetic strategy for the preparation of SnFe₂O₄/ZnO nanoparticles decorated on reduced graphene oxide (rGO), exhibiting a remarkably large surface area (120.33 m² g⁻¹). Substantial adsorption efficiency for removing MB dye was achieved, with 91.3% removal within 20 min at room temperature, and efficiencies of 79.6 to 92.8% are maintained as the pH conditions are varied from 3 to 11. Moreover, under mixed-dye conditions, involving MB, RhB, MO, RB5, and R6G organic materials, with dye concentrations ranging from 0.005 mM to 0.09 mM, an adsorption efficiency of above 50% can be reliably reached within 20 min. Such striking features can be interpreted as arising from a synergistic effect involving the hybrid composite based on a rGO matrix with negative charge and the dispersed SnFe₂O₄/ZnO nanoparticles with positive charge, additionally offering abundant adsorptive sites to allow reliable dye-adsorption kinetics.

## Introduction

In recent years, environmental pollution has increased enormously, and this is typically related to a deterioration in the quality of drinkable water all over the world.[1–3] Organic effluent containing toxic dyes may be released without undergoing careful treatment, mainly from industry, developing urban areas, and agricultural activities, including activities such as the production of leather goods, cosmetics, textiles, paper, food, plastics, consumer electronics, *etc.*[4–6] Organic dyes are regarded as serious water pollutants; they are highly soluble in aqueous solutions and are rather harmful for human beings, and they can even cause deleterious damage to the environment, simultaneously. Thus, finding a solution with ecofriendly,

reliable, and repeatable capabilities for treating pollutant dyes *via* an efficient and feasible route is in high demand. Various techniques have been investigated for the adsorption of dyes from wastewater, such as precipitation,[7] adsorption,[8] and photocatalysis,[9–14] and, among these, photocatalysis techniques seem to be the prevailing methods due to the involvement of inexpensive and facile procedures, but these approaches may create secondary pollutants in aqueous solutions.[11]

By comparison, adsorption techniques have several superior characteristics, such as the low consumption of energy, simple operation procedures, low cost, high efficiency, and excellent stability for removing various dye molecules through reliable routes.[12] So far, the most common and commercial adsorbents involve activated carbon because of its large surface area and high adsorption efficiency.[13] Nevertheless, it requires complicated synthetic procedures and is difficult to reuse for the cycled removal of dyes. Recently, two-dimensional (2D) materials have attracted extensive attention because they simultaneously possess large surface areas and abundant active sites.[14] In this regard, reduced graphene oxide (rGO) has been considered as a promising candidate for employment in dye removal due to its comparably high chemical stability and good mechanical strength, and it has also been used for many applications, including in catalysts,[15] gas sensors,[16] supercapacitors,[17] and

*ᵃDepartment of Materials Science and Engineering, National Cheng Kung University, No. 1 University Road, Tainan 70101, Taiwan. E-mail: timcychen@mail.ncku.edu.tw*

*ᵇNanotechnology & Catalysis Research Centre, Institute for Advanced Studies, University of Malaya, 50603 Kuala Lumpur, Malaysia*

*ᶜThe University of Danang, University of Science and Technology, 54 Nguyen Luong Bang, Vietnam*

*ᵈHierarchical Green-Energy Materials (Hi-GEM) Research Center, National Cheng Kung University, No. 1 University Road, Tainan 70101, Taiwan*

photodetectors.[18–20] Aside from that, semiconductor materials, such as ZnO nanocrystals, possess high potential for organic treatment because of the use of facile and inexpensive synthetic processes and their high chemical stabilities.[21] Taking all this into account, in this study, we made the first attempt to synthesize a magnetically recyclable SnFe$_2$O$_4$/ZnO@rGO hybrid nanocomposite *via* a green synthetic method, enabling the rapid removal of both cationic and anionic dyes from aqueous media through an efficient adsorption pathway; only very few literature studies have previously focused on the removal of both types of dyes *via* an adsorption route. Systematic investigations into the adsorption capabilities and mechanistic studies have been performed to allow the practical employment of this designed nanocomposite in dye treatment.

## Experimental details

### Synthesis of SnFe$_2$O$_4$ nanoparticles

SnFe$_2$O$_4$ nanoparticles were prepared *via* a co-precipitation method. In general, 88.9 mg of SnCl$_2$ and 378.8 mg of Fe(NO$_3$)$_3$·9H$_2$O at a stoichiometric ratio of 1 : 2 were dissolved in ethanol (99%) as a precursor solution. After that, 30 ml of hexane and 60 ml of aqueous NaOH solution (1 M) were added into the solution, which was kept for 4 h at room temperature. Subsequently, the precipitate was withdrawn from the solution and carefully washed with ethanol and deionized (DI) water several times. Finally, the as-prepared SnFe$_2$O$_4$ nanoparticles were dried in air at 80 °C. In addition, the use of various concentrations of precursors in the preparation process has been examined, as presented in the ESI.†

### Synthesis of SnFe$_2$O$_4$/ZnO nanoparticles

0.0275 g of zinc acetate powder was dissolved in 30 ml of ethanol (99%) under magnetic stirring at 300 rpm and 40 °C for 1 h. The precipitated ZnO nanoparticles were coated onto SnFe$_2$O$_4$ *via* a drop-coating method, and the obtained samples were heated at 80 °C for 1 h, with the procedure repeated three times. Finally, the samples were then subjected to an annealing process at 300 °C for 1 h, and the as-synthesized nanoparticles are denoted as SnFe$_2$O$_4$@ZnO.

### Synthesis of SnFe$_2$O$_4$/ZnO@rGO nanocomposites

The preparation of SnFe$_2$O$_4$/ZnO@rGO composites was based on successive ultrasonication and heat treatment. The rGO sheets were synthesized *via* a modified Hummers' method.[22] To form the nanocomposites, 1.2 M SnFe$_2$O$_4$/ZnO and rGO were dispersed in ethanol (100 ml) under ultrasonication for 30 min. The obtained precipitates were then filtered and washed with DI water and ethanol repeatedly, and the as-prepared samples were dried at 70 °C. rGO sheets at different weight ratios (5, 7, 10, 16, and 20 wt%) were introduced under magnetic stirring at 300 rpm, and the obtained products were preserved in a vacuum box (in the text, SnFe$_2$O$_4$/ZnO@rGO refers to 16 wt% rGO, unless otherwise mentioned).

### Characterization

The as-synthesized samples were characterized *via* X-ray diffraction (XRD, Bruker AXS Gmbh) using Cu Kα ($\lambda$ = 0.1540598 nm) as the radiation source. The morphologies were characterized *via* scanning electron microscopy (SEM, HITACHI SU8000). Fourier-transform infrared spectra (FTIR, PerkinElmer Frontier) were obtained to investigate the functional groups at sample surfaces. Raman spectroscopy (Renishaw, Wotton-under-Edge, UK) was used to further characterize the correlated crystal structures. The light-emitting properties of samples were examined *via* photoluminescence spectroscopy using a light-emitting diode (LED) as the light source with a center wavelength of 365 nm. The surface areas of samples were analyzed *via* Brunauer–Emmett–Teller (BET) measurements. The surface charge was evaluated with a zeta potential analytic system, and the sizes of the particles in aqueous solution were measured with a dynamic light spectrometer (DLS, DelsaNano C). Light-adsorption experiments were carried out with a UV/visible spectrometer (HITCHI U-3900H).

### Dye-adsorption measurements

For these measurements, the adsorption of various organic dyes, including methylene blue (MB), rhodamine B (RhB), methyl orange (MO), reactive black 5 (RB5), and rhodamine 6G (R6G), was examined in the presence of the various designed absorbents *via* analyzing the light-absorption spectra from 300 to 800 nm using UV-vis spectroscopy (HITACHI, U-3900H). The preparation of dye solutions was conducted *via* dissolving 120 mg of adsorbent in 20 ml of aqueous dye solution, and all adsorption tests were performed at room temperature (25 °C) under dark conditions. The adsorption characteristics were evaluated with the following equation:[23]

$$\text{Adsorption (\%)} = [(C_i - C_e)/C_i] \times 100 \tag{1}$$

where $C_i$ and $C_e$ are the initial concentration and equilibrium concentration of the organic dye, respectively. The adsorbent stability of the hybrid nanocomposites was examined *via* conducting recycling tests. After each adsorption test, the nanocomposite was separated from the dye solution *via* an external magnet. The adsorbent was then washed with DI water and ethanol several times, followed by drying at 40 °C for 0.5 h. Subsequently, the dried sample was subjected to the next cycle of adsorption testing. All adsorption tests were performed five times, and average values are demonstrated.

## Results and discussion

The XRD spectra of samples are presented in Fig. 1(a), including rGO, SnFe$_2$O$_4$, and the SnFe$_2$O$_4$/ZnO@rGO nanocomposite. From an examination of the XRD patterns, the sharp peak at a $2\theta$ value of 26.30° can be assigned to the (002) plane of rGO.[24] In addition, the peaks at $2\theta$ values of 30.2°, 35.6°, 44.09°, 53.3°, and 62.6° correspond to the (220), (311), (400), (422), and (440) planes of spinel SnFe$_2$O$_4$ crystals, respectively.[25] The crystalline diffraction signals at $2\theta$ values of 32.03°, 32.9°, 38.8°, 47.2°, 55.7°, 62.7°, and
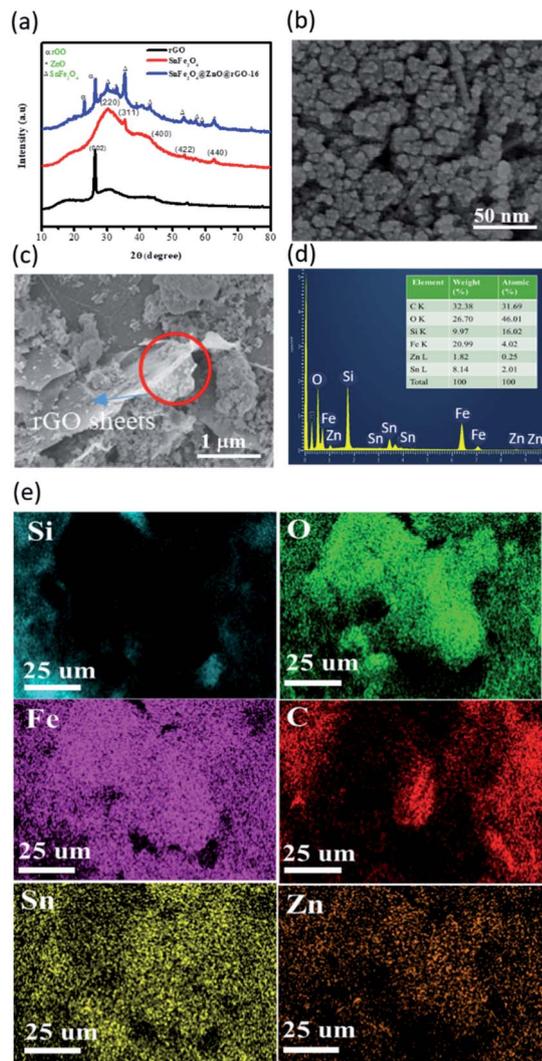
Fig. 1 (a) XRD patterns of various samples. Representative SEM images of (b) $SnFe_2O_4/ZnO$ nanoparticles and (c) the $SnFe_2O_4/ZnO@rGO$ nanocomposite. (d) Elemental analysis and (e) EDS mapping of the $SnFe_2O_4/ZnO@rGO$ nanocomposite.

74.2° represent the (100), (002), (101), (102), (110), (103), and (200) crystallographic planes, respectively, of the wurtzite structure of ZnO. In addition, the related lattice constants of ZnO in $SnFe_2O_4/ZnO@rGO$ samples with different amounts of rGO can be evaluated using the hexagonal space lattice equation:[26]

$$\frac{1}{d^2} = \frac{4}{3}\frac{h^2 + hk + k^2}{a^2} + \frac{l^2}{c^2} \quad (2)$$

where $d$ is the interplanar distance; $h$, $k$, and $l$ represent the Miller indices of the hexagonal plane; and $a$ and $c$ are the lattice constants of the hexagonal structure. Furthermore, the grain size of the related nanostructures can be evaluated with the Scherrer equation:[27]

$$t = \frac{k\lambda}{\beta \cos\theta} \quad (3)$$

where $t$ and $K$ are the crystal size and dimensionless shape factor, respectively; $\lambda$ and $\beta$ are the wavelength of the X-ray used

and the correlated full-width-at-half-maximum (FWHM) intensity of the XRD peak, respectively; and $\theta$ represents the Bragg angle of diffraction. Both the lattice constants and crystal sizes for the components and a hybrid nanostructure are presented in Table 1. Accordingly, it can be found that the crystallite configurations in terms of the lattice parameters of both the rGO and $SnFe_2O_4$ components in the $SnFe_2O_4/ZnO@rGO$ nanocomposite do not show any obvious variations in comparison with the pure rGO and $SnFe_2O_4$ phases, confirming the preserved crystallinity of the $SnFe_2O_4/ZnO@rGO$ composites synthesized *via* a facile co-precipitation method. Moreover, upon the combination of ZnO and $SnFe_2O_4$, the crystallite size of the $SnFe_2O_4$ lattice is increased, whereas the grain size of rGO remains almost consistent in comparison with the precursor, which implies that the change in crystal size from $SnFe_2O_4$ can mainly be attributed to the incorporation of ZnO nanoparticles. From examinations of the preferential crystallographic orientations of both involved crystals, the crystallites of the ZnO nanoparticles are highly oriented with respect to the $SnFe_2O_4$ matrix due to the existence of trivial lattice mismatch between $SnFe_2O_4$ and ZnO ($\sim$6%), where stress relaxation at the boundaries of $SnFe_2O_4$ crystals can in turn cause an increase in crystallite size, which may contribute to the sound magnetization characteristics allowing the recycling of the absorbents for dye removal, as shown in the ESI.†

The morphology of the $SnFe_2O_4@ZnO$ composite, obtained *via* SEM, is shown in Fig. 1(b). The results suggest the rough features of the nanocomposites, with average dimensions of 14 $\pm$ 0.5 nm. Also, upon introducing rGO sheets as a support with a large surface area for the formation of a hybrid adsorbent, one can clearly find that $SnFe_2O_4@ZnO$ nanoparticles are decorated on the rGO sheets, creating a composite structure with a dense configuration (Fig. 1(c)), which is highly beneficial for the adsorption of organic dyes from aqueous media.[28] In addition, the corresponding chemical composition of the as-synthesized composite is examined based on EDS mapping and spectral analysis, as indicated in Fig. 1(d) and (e), respectively, evidencing the uniform decoration of $SnFe_2O_4/ZnO$ on the rGO support. The quantitative results further indicate clearly that the atomic ratio of Sn to Fe is 1 : 2, which corresponds to the stoichiometry of the $SnFe_2O_4$ crystals, as demonstrated in the

Table 1 An evaluation of the crystal sizes and lattice parameters of various samples

| Sample | Crystal size (nm) | Lattice parameter (Å) | |
|---|---|---|---|
| | X-ray diffraction | | |
| | | $a$ | $c$ |
| rGO | 13.96 | N/A | 6.77 |
| $SnFe_2O_4$ | 0.83 | 8.363 | N/A |
| **$SnFe_2O_4/ZnO@rGO$** | | | |
| rGO | 14.09 | N/A | 6.75 |
| $SnFe_2O_4$ | 1.56 | 8.308 | N/A |
| ZnO | 1.66 | 3.224 | 5.44 |

inset figure of Fig. 1(d). In addition, the existence of Zn and C elements also shows that the formed composite contains ZnO decoration and supporting rGO sheets. In addition, the chemical states of the nanocomposites were further analyzed *via* XPS investigations, as presented in the ESI.†

To further explore the crystal features of the nanocomposite, Raman spectra of samples were obtained, as shown in Fig. 2(a). Clearly, two dominant Raman peaks exist, located at 1332.4 cm$^{-1}$ (D band) and 1574.1 cm$^{-1}$ (G band), where the D band correlates with structural defects in the hexagonal graphitized structure and the G band represents the ordered graphite lattices.[29] In SnFe$_2$O$_4$@rGO form, the corresponding intensity ratio in terms of $I_D/I_G$ is 0.25, which is comparable with pure rGO ($I_D/I_G$ = 0.29). For the SnFe$_2$O$_4$/ZnO@rGO composite, the lowest value of $I_D/I_G$ (0.14) of the three tested samples can be found. In addition, both the D and G band values are spectrally shifted to lower Raman shift values, which suggests a reduction in the number of oxygen functional groups in GO and the restoration of new graphitic domains from the amorphous region of GO. Thus, the red shifting of the characteristic Raman peaks and the rather low $I_D/I_G$ value compared with pure rGO and SnFe$_2$O$_4$/rGO are evidence that the structural defects of rGO sheets are effectively negated upon the incorporation of SnFe$_2$O$_4$/ZnO, which may originate from the existence of energetically favorable sites at the structural defects of rGO that support the nucleation of SnFe$_2$O$_4$ seeds at these locations.

The surface features are characterized *via* FTIR analysis, as demonstrated in Fig. 2(b). The peak from rGO appearing at 1632 cm$^{-1}$ is assigned to conjugate C=C skeletal stretching vibrations from the sp$^2$ bonding of carbon structures.[25] In the SnFe$_2$O$_4$ sample, the broad peaks at vibration modes of both 3446.7 cm$^{-1}$ and 1641 cm$^{-1}$ belong to the stretching vibrations of –OH bond. In addition, the peaks at 557 cm$^{-1}$ and 440 cm$^{-1}$

are the signals of Sn–O and Fe–O bonds, respectively, clearly evidencing the formation of crystalline SnFe$_2$O$_4$ lattices. In addition, the absorption peak at 402 cm$^{-1}$ is assigned to the stretching vibrations of Zn–O bonds in tetrahedral positions.[30] Moreover, a weak characteristic peak occurring at around 1623 cm$^{-1}$ originates from the conjugate C=C skeletal stretching vibrations of rGO in the SnFe$_2$O$_4$/ZnO@rGO composite, and the above results indicate the successful formation of a hybrid nanocomposite. The light-absorption spectra were examined, as shown in Fig. 2(c). ZnO demonstrates a single absorption band below 378 nm, which corresponds well with the literature.[31,32] Meanwhile, stronger absorption in the visible region can be observed from SnFe$_2$O$_4$ powder, presenting a dark brown color, as shown in the inset of Fig. 2(c), whereas rGO does not present absorption characteristics in the examined wavelength range. The incorporation of SnFe$_2$O$_4$/ZnO nanoparticles with rGO sheets leads to a substantial increase in light absorption due to two possible reasons. First, the composite structure possesses a comparably large surface area and rough features; thus, incoming light may undergo multiple reflection and scattering processes, facilitating the reabsorption of light and further enhancing the light absorption over the entire spectral region. Moreover, rGO sheets have a higher refractive index (2.7–3.1) in the visible region than at UV wavelengths, thus trapping incident and unabsorbed light inside the nanocomposite, which is reflected in the additional absorption of light at long wavelengths (450–600 nm). In addition, the light-emitting characteristics of samples are presented in the ESI.†

In addition, an examination of zeta potentials was carried out to reveal the surface charge of particles dispersed in an aqueous medium, as shown in Fig. 2(d). It can be observed that the zeta potentials of SnFe$_2$O$_4$/ZnO@rGO at different environmental pH values were measured, indicating that the involved surface charge remains negative when the pH is in the range of 3 to 11, which implies that the material can reliably absorb cationic dyes, regardless of variations of pH in aqueous media. Furthermore, the tested nanocomposites, including SnFe$_2$O$_4$@rGO and SnFe$_2$O$_4$/ZnO@rGO nanocomposites, display highly negative charge at the composite surfaces, with values of −85.6 mV and −70.8 mV, respectively, under environmental conditions of pH 7. In comparison with SnFe$_2$O$_4$ nanoparticles alone, with a relatively small negative zeta potential (−51.6 mV), these findings explicitly show that the existence of rGO in the nanocomposites can substantially provide negative charge at the nanocomposite surface.

To examine the surface areas of the absorbents, BET investigations are performed. The adsorption–desorption isotherm
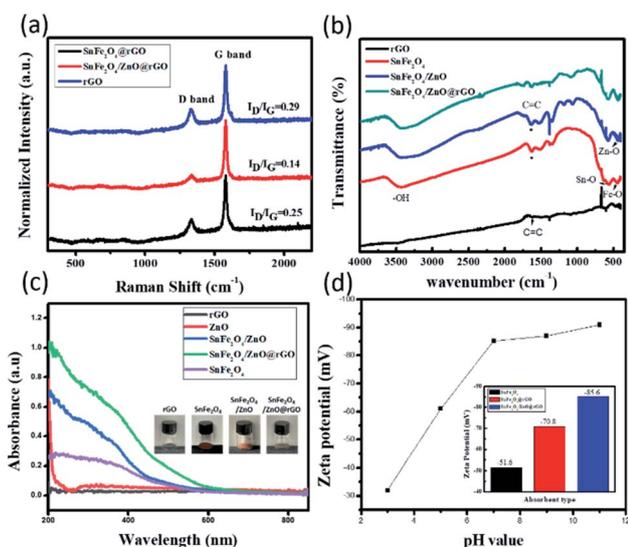


**Fig. 2** (a) Raman spectra, (b) FTIR analysis and (c) light-absorption spectra of various adsorbent samples. (d) Measurements of the zeta potential of the SnFe$_2$O$_4$/ZnO@rGO nanocomposite in various pH environments. The inset of (d) shows the zeta potentials of three different samples at a pH level of 7.

**Table 2** The measured BET analysis results

| Sample | Surface area (m$^2$ g$^{-1}$) | Pore volume (cm$^3$ g$^{-1}$) | Pore size (nm) |
|---|---|---|---|
| SnFe$_2$O$_4$/ZnO | 79.60 | 0.206 | 7.17 |
| SnFe$_2$O$_4$@rGO | 114.88 | 0.297 | 14.34 |
| SnFe$_2$O$_4$/ZnO@rGO | 120.33 | 0.335 | 16.1 |

($N_2$) of the SnFe$_2$O$_4$/ZnO@rGO nanocomposites, where the measured curves all correspond to the phenomenon of capillary agglomeration in porous adsorbents,[33] are presented in the ESI.† Such features have been reported as being beneficial for the substantial enhancement of dye-adsorption characteristics.[34] Accordingly, the specific surface areas of different samples are evaluated, as displayed in Table 2. The results indicate that SnFe$_2$O$_4$/ZnO@rGO possesses the largest specific surface area (120.33 m$^2$ g$^{-1}$), approximately 1.51 and 1.04 times larger than those of SnFe$_2$O$_4$/ZnO (79.60 m$^2$ g$^{-1}$) and SnFe$_2$O$_4$@rGO (114.88 m$^2$ g$^{-1}$), respectively. The greatly enlarged surface area can be attributed to the incorporation of rGO, with two-dimensional structural features; also, ZnO decoration on SnFe$_2$O$_4$ nanoparticles initiates the formation of rough features, further benefiting an increase in the nanocomposite surface area. Thus, these combined effects may facilitate the creation of more active sites for allowing the effective adsorption of dye molecules.

To explore the adsorption characteristics toward organic dyes, systematic investigations with different adsorbent types, dye species and concentrations, dye mixtures, and pH values were carried out under dark conditions at room temperature. Fig. 3(a) shows the adsorption efficiencies toward MB dye at room temperature in the presence of various samples, including pure rGO, SnFe$_2$O$_4$, SnFe$_2$O$_4$/ZnO, and the SnFe$_2$O$_4$/ZnO@rGO nanocomposite. One can observe that the adsorption capabilities during a 20 min process reach 91.3% in the presence of the SnFe$_2$O$_4$/ZnO@rGO nanocomposite, whereas adsorption efficiencies of 69.7%, 57.8%, and 46.2% are obtained for pure rGO, the SnFe$_2$O$_4$@ZnO composite, and the SnFe$_2$O$_4$ nanoparticles, respectively. The substantial improvement in terms of the dye adsorption of MB molecules can be interpreted as arising from a synergistic effect involving the hybrid composite upon incorporating SnFe$_2$O$_4$/ZnO with the rGO matrix. First, the rGO support provides dual functionality for facilitating dye adsorption, which is not merely contributed to by strong π–π electron coupling between the configured benzene rings of rGO and the C=C groups of MB dye, but is also further promoted due to ionic attraction between the existing highly negative charge at the absorbent surface and cationic MB dye with a surficial positive charge. In addition, the combined structure has a comparably larger surface area, further providing more active sites that are energetically favorable for dye adsorption. Moreover, ZnO decoration also contributes to dye adsorption because of naturally occurring oxygen defects at the surface that favor attracting anionic dyes. These findings are further supported via examining the effects of environmental pH values, as demonstrated in the ESI.† The results show that the dye-adsorption efficiency of the SnFe$_2$O$_4$/ZnO@rGO nanocomposite increases from 79.6 to 92.8% when the pH is increased from 3 to 11. Thus, these hybrid composites are able to potentially treat dye mixtures containing both anionic and cationic dye groups, making them more practical for commercial use.

In addition, the optimal amount of rGO for dye adsorption was examined via varying the weight percentage of rGO from 5–20 wt%, as presented in Fig. 3(b). It should be noted that the excess addition of rGO for the preparation of composites (>16%) causes significant aggregation of the adsorptive rGO sheets, thus degrading the adsorption performances. All rGO-based nanocomposites demonstrate sound dye adsorption capabilities of over 50% within a short period (20 min), while the most efficient sample for MB adsorption has 16 wt% rGO as a support, with the dye removal efficiency reaching 91.3%. In addition, various MB dye concentrations were also examined in the presence of the SnFe$_2$O$_4$/ZnO@rGO nanocomposite, as shown in the ESI.† The dye adsorption capabilities remain higher than 80% over a wide range of dye concentrations from 0.001–0.007 mM, and no clear saturation in the presence of high concentrations of dyes is observed, indicating potential practical use for treating wastewater.

Next, different dye species were tested to envision the adsorption capabilities of this hybrid nanocomposite, as shown in Fig. 3(c). The results show the removal efficiencies of MB dye (90.2%), RhB dye (85.6%), MO dye (75.8%), RB5 dye (71.2%), and R6G dye (82.3%) after a 20 min adsorption process. The explicit dependence of the dye-adsorption rate on the dye species can mainly be attributed to the nature of the surface ionic charge and the molecular size of the organic dye involved. From zeta-potential measurements, it has been confirmed that the designed SnFe$_2$O$_4$/ZnO@rGO adsorbent has comparably higher negative charge at the surface out of the tested samples, which thus allows it to readily adsorb cationic dyes, including MB, RhB, and R6G dyes, through strong coulombic attraction, facilitating effective adsorption dynamics. Thus, relatively
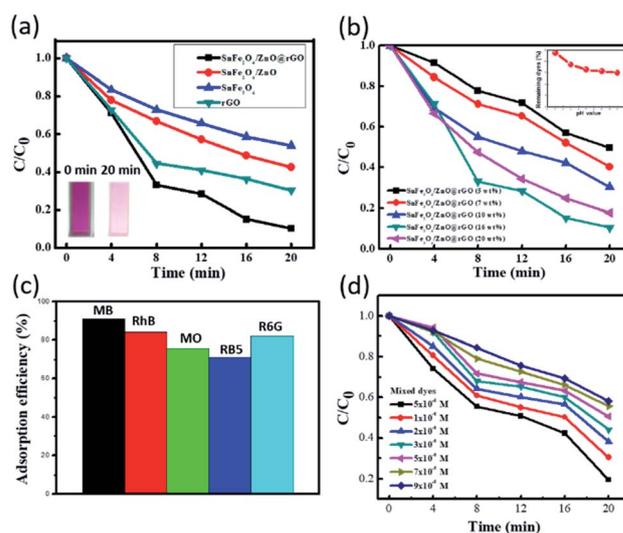


Fig. 3 The measured adsorption efficiencies of (a) various absorbent materials in the presence of MB dye, (b) SnFe$_2$O$_4$/ZnO@rGO nanocomposite samples with different amounts of rGO as the matrix in the presence of MB dye, (c) the SnFe$_2$O$_4$/ZnO@rGO (16 wt% rGO) nanocomposite in the presence of various dyes, and (d) the SnFe$_2$O$_4$/ZnO@rGO nanocomposite with different concentrations of mixed dye solutions containing MB, RhB, MO, RB5, and R6G with similar concentration ratios. The inset in (a) presents photographs of solutions containing MB dye before (0 min) and after (20 min) conducting an adsorption experiment using SnFe$_2$O$_4$/ZnO@rGO as the absorbent. The inset in (b) presents the change in adsorption performance with pH for SnFe$_2$O$_4$/ZnO@rGO.

larger adsorption efficiencies are realized in the presence of cationic organic materials compared with anionic dyes, including the MO and RB5 species tested here. In addition, examinations of dye adsorption involving mixed cationic dyes, including MB, RhB, and R6G dyes, and anionic dyes, including MO and RB5 dyes, also support these findings, as presented in the ESI.† Moreover, another dominant feature affecting the dye adsorption efficiency is the molecular weight of the dye; small molecules are more favorably adsorbed by the nanocomposite due to less steric hindrance, thus presenting sequences in terms of adsorption efficiency as follows: MB (molecular weight ($M$) = 319.85 g mol$^{-1}$) > RhB ($M$ = 479 g mol$^{-1}$) > R6G ($M$ = 479.02 g mol$^{-1}$) in the cationic category; and MO ($M$ = 327.33 g mol$^{-1}$) > RB5 ($M$ = 427.33 g mol$^{-1}$) in the anionic category.

Aside from examinations involving single dye species, Fig. 3(d) shows the adsorption performance of the SnFe$_2$O$_4$/ZnO@rGO nanocomposite in the presence of mixtures of cationic and anionic dyes containing MB, RhB, MO, RB5, and R6G dyes with similar relative concentrations; the total dye concentrations were varied in the range of 0.005 mM to 0.09 mM. The adsorption efficiencies remain above 50%, while engagement with a wide range of dye concentrations is encountered. Specifically, a slight reduction of less than 32% is observed in terms of adsorption efficiency as the dye concentration is increased from 0.005 mM to 0.09 mM. Such striking features imply the existence of a synergistic effect relating to the kinetics of dye adsorption on the hybrid composites. The dye adsorption kinetics can be limited by different factors, *e.g.*, the adsorption process may be ceased due to the aggregation of dye on the absorbent surface, causing a screening effect against ionic attraction between the dye and absorbent. Nevertheless, in the designed hybrid nanocomposites, the uniformly distributed SnFe$_2$O$_4$/ZnO nanostructures are decorated on rGO sheets with a high surface area; these features facilitate the inhibition of the aggregation of highly concentrated dyes directly at specific positions due to the existence of abundant adsorptive sites. In turn, the surface of the absorbent stays active for the successful and long-term effective adsorption of organic dyes.

To explore the dynamic adsorption characteristics and elucidate the underlying kinetic mechanism, three different adsorption-isotherm models, the Langmuir, Freundlich, and Dubinin–Radushkevich (D–R) isotherm models, are employed. In general, the Langmuir isotherm model expresses the formation of a monolayer adsorbate on the outer surface of an adsorbent, which is particularly valid when there is a finite number of sites that are energetically capable of molecule adsorption and the acquired energy for initiating the adsorption process is identical at all active sites on the absorbent surface; the model is presented in eqn (4):[35]

$$C_e/Q_e = (C_e/Q_m) + 1/Q_m K_L \quad (4)$$

where $Q_e$ is the adsorbed quantity of dye, $C_e$ is the equilibrium solute concentration, $Q_m$ is the maximum adsorption capacity, and $K_L$ is the equilibrium constant of the Langmuir isotherm. The Freundlich isotherm model is adopted to interpret dye adsorption on heterogeneous surfaces, which is applicable for

the occurrence of multilayer adsorption over heterogeneous features; the model is described in eqn (5):[36]

$$\log(Q_e) = \log(K_f) + 1/n \log(C_e) \quad (5)$$

where $K_f$ and $n$ are the Freundlich isotherm constant and a constant related to the heterogeneity of the adsorbent surface, respectively. The D–R model is associated with a Gaussian distribution of active sites for dye adsorption, which is readily applicable for differentiating two competing kinetic processes, including the chemical adsorption and physical adsorption of metal ions;[37] the kinetic model is expressed in eqn (6):

$$\ln Q_e = \ln Q_{DR} + Ke^2 \quad (6)$$

where $K$ and $e$ are the Polanyi potential and Dubinin–Radushkevich constant, respectively. Accordingly, the fitting results of the Langmuir isotherm adsorption model (Fig. 4(a)), Freundlich isotherm model (Fig. 4(b)) and D–R isotherm adsorption model (Fig. 4(c)) can be quantitatively distinguished based on the corresponding linear regression coefficient ($R^2$) values, where the $R^2$ value shows the best value (0.99) from the Freundlich isotherm adsorption model in comparison with the Langmuir and D–R models, where values of 0.55 and 0.93, respectively, were obtained. This clearly indicates that the underlying kinetics in the presence of the SnFe$_2$O$_4$/ZnO@rGO nanocomposite can mainly be attributed to the heterogeneous adsorption of dyes, which is contributed to by synergistic effects involving the hybrid SnFe$_2$O$_4$/ZnO@rGO nanocomposite. Moreover, cycling tests to show the reuse capabilities of the hybrid adsorbent are demonstrated in Fig. 4(d). It can be found that the reduction in adsorption efficiency in the presence of SnFe$_2$O$_4$/ZnO@rGO remains less than 6% after the repeated utilization of the absorbent for five cycles, verifying its reliability for wastewater treatment.

The overall process of dye removal is schematically illustrated in Fig. 4(e), comparing a typical rGO structure and the hybrid nanocomposite. It is found that only cationic dyes can be effectively adsorbed on the rGO surface surrounded by highly negative
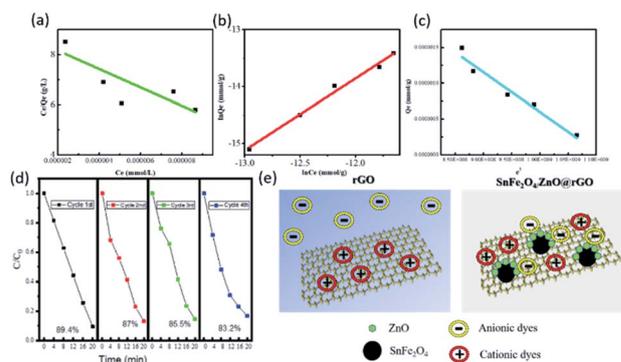
**Fig. 4** Adsorption results in the presence of the nanocomposite adsorbent fitted using various kinetic isotherm models: (a) Langmuir, (b) Freundlich, and (c) Dubinin–Radushkevich isotherm models. (d) Cycling tests involving the SnFe$_2$O$_4$/ZnO@rGO nanocomposite. (e) A schematic diagram of the evolution of the adsorption mechanism when treating mixed cationic and anionic dyes.

**Table 3** A comparison of separable absorbents for the removal of organic dyes

| No. | Adsorbent | Dye | Adsorption efficiency (%) | Time (min) | Concentration of dye | Reference |
|---|---|---|---|---|---|---|
| 1 | $MoS_2$ | MB | 99 | 180 | $3.2 \times 10^{-5}$ M | 38 |
| 2 | $rGO-Fe_3O_4$ | RhB | 50 | 360 | $1.5 \times 10^{-5}$ M | 39 |
| 3 | AC | MB | 98.0–99.6 | 300 | 40–120 mg $L^{-1}$ | 40 |
|   | GO |  | 94.8–98.8 |  |  |  |
|   | CNTs |  | 72.4–82.7 |  |  |  |
| 4 | ZnO–Si@rGO | MB | 59 | 120 | $3.4 \times 10^{-6}$ M | 41 |
| 5 | Magnetic graphene–$Fe_3O_4$@carbon (GFC) | MB | 97.8 | 120 | $1.5 \times 10^{-4}$ M | 42 |
| 6 | $Fe_3O_4$ | MB | 7 | 120 | $3.1 \times 10^{-5}$ M | 29 |
|   | $ZnFe_2O_4$ |  | 15 |  |  |  |
|   | $Fe_3O_4$–rGO |  | 60 |  |  |  |
|   | $ZnFe_2O_4$–rGO |  | 82 |  |  |  |
|   | Pure rGO |  | 83 |  |  |  |
| 7 | $SnFe_2O_4$/ZnO@rGO | MB | 90.2 | 20 | $5 \times 10^{-5}$ M | This work |
|   |  | Mixed dyes (MB, RhB, MO, RB5, and R6B) | 58.3 | 20 | $9 \times 10^{-6}$ M |  |

charge through ionic attraction between dyes and the rGO absorbent; anionic dyes are coulombically repelled from the rGO sheets and eventually remain in the aqueous medium. Nevertheless, this challenge can be effectively overcome with the incorporation of a hybrid absorbent, where ZnO-decorated $SnFe_2O_4$ allows the separate absorption of anionic dyes, thus allowing the beneficial and efficient separation of organic dyes. Moreover, such incorporation of a rGO matrix, owning negative charge, with dispersed $SnFe_2O_4$/ZnO nanoparticles, with positive charge, additionally yields abundant adsorptive sites due to the large surface area and, in turn, the surface of the absorbent stays active, providing a long-term and reliable pathway for practically treating different types of wastewater. To further demonstrate the remarkable adsorption capabilities of the designed nanocomposite, recent reports regarding the study of magnetically separable absorbents for dye adsorption are summarized in Table 3; the time required for dye adsorption using the $SnFe_2O_4$/ZnO@rGO nanocomposite was substantially reduced to 20 min compared with other reported adsorbent materials. The results verify the superior efficiency and sound reliability of the designed nanocomposite for dye adsorption, and this may potentially allow for the practical treatment of versatile organic species.

## Conclusions

Magnetically separable $SnFe_2O_4$/ZnO nanoparticles decorated on rGO sheets with a remarkably large surface area (120.33 $m^2$ $g^{-1}$) have been prepared *via* a green synthetic method. Detailed crystallographic, morphological, surface-feature, and light-absorption investigations reveal the successful formation of this hybrid nanocomposite, and the red shifting of the characteristic Raman peaks and the rather low $I_D/I_G$ value compared with pure rGO and $SnFe_2O_4$/rGO evidence the fact that the structural defects of the rGO sheets are effectively negated upon the incorporation of $SnFe_2O_4$/ZnO nanoparticles. The adsorption efficiency toward MB dye in the presence of the designed

$SnFe_2O_4$/ZnO@rGO nanocomposite can reach 91.3% within 20 min at room temperature, and efficiencies of 79.6 to 92.8% are maintained when the pH value is varied from 3 to 11. Moreover, in the presence of a mixture of dyes containing MB, RhB, MO, RB5, and R6G organic materials, with dye concentrations ranging from 0.005 mM to 0.09 mM, the adsorption efficiencies can be efficiently maintained above 50% after treatment for 20 min. The underlying kinetics of dye adsorption are examined, indicating that the Freundlich isotherm adsorption model, with an $R^2$ value of 0.99, is most suitable, suggesting a heterogeneous adsorption route. A synergistic effect supporting the effective adsorption of organic dyes allows such superior adsorption efficiency; the constituted rGO matrix provides an ultra-large surface area with negative charge that enables the trapping of cationic dyes through ionic attraction, while the ZnO seeds decorated on $SnFe_2O_4$ nanoparticles possess positive charge, facilitating the adsorption of anionic dyes. These combined features yield superior efficiency and sound reliability compared with other absorbent materials, and this material has high potential for the practical treatment of different types of wastewater in an ecofriendly and reliable way.

## Conflicts of interest

There are no conflicts of interest to declare.

## Acknowledgements

Science and Technology, National Cheng Kung University for the facilities provided for conducting material characterization studies.

# Notes and references

1  M. M. Mohamed, M. Khairy and S. Eid, Activity and stability studies of titanates and titanate-carbon nanotubes supported Ag anode catalysts for direct methanol fuel cell, *J. Power Sources*, 2016, **304**, 255–265.

2  S. Thangavel, S. Thangavel, N. Raghavan, K. Krishnamoorthy and G. Venugopal, Visible-light driven photocatalytic degradation of methylene-violet by rGO/Fe$_3$O$_4$/ZnO ternary nanohybrid structures, *J. Alloys Compd.*, 2016, **665**, 107–112.

3  B. Ma, R. Cong, W. Gao and T. Yang, Photocatalytic overall water splitting over an open-framework gallium borate loaded with various cocatalysts, *Catal. Commun.*, 2015, **71**, 17–20.

4  F. Han, V. S. R. Kambala, M. Srinivasan, D. Rajarathnam and R. Naidu, Tailored titanium dioxide photocatalysts for the degradation of organic dyes in wastewater treatment: a review, *Appl. Catal., A*, 2009, **359**, 25–40.

5  H. Chen, J. Zhao, J. Wu and G. Dai, Isotherm., thermodynamic, kinetics and adsorption mechanism studies of methyl orange by surfactant modified silkworm exuviae, *J. Hazard. Mater.*, 2011, **192**, 246–254.

6  F. Liu, Y. H. Leung, A. B. Djurisic, A. M. C. Ng and W. K. Chan, Native defects in ZnO: effect on dye adsorption and photocatalytic degradation, *J. Phys. Chem. C*, 2013, **117**, 12218–12228.

7  M. Toor and B. Jin, Adsorption characteristics, isotherm, kinetics, and diffusion of modified natural bentonite for removing diazo dye, *Chem. Eng. J.*, 2012, **187**, 79–88.

8  J. Zhu, Y. Wang, J. Liu and Y. Zhang, Facile one-pot synthesis of novel spherical zeolite–reduced graphene oxide composites for cationic dye adsorption, *J. Ind. Eng. Chem.*, 2014, **53**, 13711–13717.

9  C.-Y. Chen, P.-H. Hsiao, T.-C. Wei, T.-C. Chen and C.-H. Tang, Well incorporation of carbon nanodots with silicon nanowire arrays featuring excellent photocatalytic performances, *Phys. Chem. Chem. Phys.*, 2017, **19**, 11786–11792.

10  C.-H. Tang, P.-H. Hsiao and C.-Y. Chen, Efficient Photocatalysts Made by Uniform Decoration of Cu$_2$O Nanoparticles on Si Nanowire Arrays with Low Visible Reflectivity, *Nanoscale Res. Lett.*, 2018, **13**, 1–8.

11  Z. Chen, S. Liu, M.-Q. Yang and Y.-J. Xu, Synthesis of uniform CdS nanospheres/graphene hybrid nanocomposites and their application as visible light photocatalyst for selective reduction of nitro organics in water, *ACS Appl. Mater. Interfaces*, 2013, **5**, 4309–4319.

12  C.-Y. Chen, M.-C. Cheng and A.-H. Chen, Photocatalytic decolorization of remazol black 5 and remazol brilliant orange 3R by mesoporous TiO$_2$, *J. Environ. Manage.*, 2012, **102**, 125–133.

13  Y. Lu, M. Jiang, C. Wang, Y. Wang and W. Yang, Effects of matrix and functional groups on tylosin adsorption onto resins and carbon nanotubes, *Water, Air, Soil Pollut.*, 2013, **224**, 1–12.

14  A. K. Geim and K. S. Novoselov, in *Nanoscience and technology: a collection of reviews from nature journals*, World Scientific, 2010, pp. 11–19.

15  R. Xu, H. Bi, G. He, J. Zhu and H. Chen, Synthesis of Cu-Fe$_3$O$_4$@ graphene composite: a magnetically separable and efficient catalyst for the reduction of 4-nitrophenol, *Mater. Res. Bull.*, 2014, **57**, 190–196.

16  L. Zhou, F. Shen, X. Tian, D. Wang, T. Zhang and W. Chen, Stable Cu$_2$O nanocrystals grown on functionalized graphene sheets and room temperature H$_2$S gas sensing with ultrahigh sensitivity, *Nanoscale*, 2013, **5**, 1564–1569.

17  S. Chen, J. Zhu, X. Wu, Q. Han and X. Wang, Graphene oxide–MnO$_2$ nanocomposites for supercapacitors, *ACS Nano*, 2010, **4**, 2822–2830.

18  Z. Zhan, L. Zheng, Y. Pan, G. Sun and L. Li, Self-powered, visible-light photodetector based on thermally reduced graphene oxide–ZnO (rGO–ZnO) hybrid nanostructure, *J. Mater. Chem. A*, 2012, **22**, 2589–2595.

19  P.-H. Hsiao, Y.-C. Lai and C.-Y. Chen, Dual-sized carbon quantum dots enabling outstanding silicon-based photodetectors, *Appl. Surf. Sci.*, 2021, **542**, 148705.

20  P.-H. Hsiao, T.-C. Wei and C.-Y. Chen, Stability improvement of Cu(ii)-doped ZnS/ZnO photodetectors prepared with a facile solution-processing method, *Inorg. Chem. Front.*, 2021, **8**, 311.

21  H. Li, Y. Wei, Y. Zhang, C. Zhang, G. Wang, Y. Zhao, F. Yin and Z. Bakenov, In situ sol-gel synthesis of ultrafine ZnO nanocrystals anchored on graphene as anode material for lithium-ion batteries, *Ceram. Int.*, 2016, **42**, 12371–12377.

22  W. S. Hummers Jr and R. E. Offeman, Preparation of graphitic oxide, *J. Am. Chem. Soc.*, 1958, **80**, 1339.

23  E. C. Lima, A. Hosseini-Bandegharaei, J. C. Moreno-Piraján and I. Anastopoulos, A critical review of the estimation of the thermodynamic parameters on adsorption equilibria. Wrong use of equilibrium constant in the Van't Hoof equation for calculation of thermodynamic parameters of adsorption, *J. Mol. Liq.*, 2019, **273**, 425–434.

24  R. Aradhana, S. Mohanty and S. K. Nayak, Comparison of mechanical, electrical and thermal properties in graphene oxide and reduced graphene oxide filled epoxy nanocomposite adhesives, *Polymer*, 2018, **141**, 109–123.

25  J. Luo, Z. Yan, R. Liu, J. Xu and X. Wang, Synthesis and excellent visible light photocatalysis performance of magnetic reduced graphene oxide/ZnO/ZnFe$_2$O$_4$ composites, *RSC Adv.*, 2017, **7**, 23246–23254.

26  M. H. Shams, A. S. Rozatian, M. H. Yousefi, J. Valíček and V. Šepelák, Effect of Mg$^{2+}$ and Ti$^{4+}$ dopants on the structural, magnetic and high-frequency ferromagnetic properties of barium hexaferrite, *J. Magn. Magn. Mater.*, 2016, **399**, 10–18.

27  P. Scherrer, in *Kolloidchemie Ein Lehrbuch*, Springer, 1912, pp. 387–409.

28  J. Zhang, R. Shu, C. Guo, R. Sun, Y. Chen and J. Yuan, Fabrication of nickel ferrite microspheres decorated multi-walled carbon nanotubes hybrid composites with

enhanced electromagnetic wave absorption properties, *J. Alloys Compd.*, 2019, **784**, 422–430.

29 F. Jumeri, H. Lim, S. Ariffin, N. Huang, P. Teo, S. Fatin, C. Chia and I. Harrison, Microwave synthesis of magnetically separable $ZnFe_2O_4$-reduced graphene oxide for wastewater treatment, *Ceram. Int.*, 2014, **40**, 7057–7065.

30 P. Laokul, V. Amornkitbamrung, S. Seraphin and S. Maensiri, Characterization and magnetic properties of nanocrystalline $CuFe_2O_4$, $NiFe_2O_4$, $ZnFe_2O_4$ powders prepared by the Aloe vera extract solution, *Curr. Appl. Phys.*, 2011, **11**, 101–108.

31 C.-H. Tang, K.-Y. Chen and C.-Y. Chen, Solution-processed ZnO/Si based heterostructures with enhanced photocatalytic performance, *New J. Chem.*, 2018, **42**, 13797–13802.

32 P.-H. Hsiao, T.-C. Li and C.-Y. Chen, $ZnO/Cu_2O/Si$ Nanowire Arrays as Ternary Heterostructure-Based Photocatalysts with Enhanced Photodegradation Performances, *Nanoscale Res. Lett.*, 2019, **14**, 1–8.

33 A. Ramadani, Y. Stiadi, N. Jamarun and S. Arief, Photocatalytic Performance of $ZnO–ZnFe_2O_4$ Magnetic Nanocomposites on Degradation of Congo Red Dye Under Solar Light Irradiation, *J. Mater. Environ. Sci.*, 2017, **8**, 1634–1643.

34 H.-Y. Zhu, R. Jiang, Y.-Q. Fu, R.-R. Li, J. Yao and S.-T. Jiang, Novel multifunctional $NiFe_2O_4/ZnO$ hybrids for dye removal by adsorption, photocatalysis and magnetic separation, *Appl. Surf. Sci.*, 2016, **369**, 1–10.

35 Y. Lin, H. Chen, K. Lin, B. Chen and C. Chiou, Application of magnetic particles modified with amino groups to adsorb

36 J. Anwar, U. Shafique, M. Salman, A. Dar and S. Anwar, Removal of Pb(II) and Cd(II) from water by adsorption on peels of banana, *Bioresour. Technol.*, 2010, **101**, 1752–1755.

37 A. Dada, A. Olalekan, A. Olatunya and O. Dada, Langmuir, Freundlich, Temkin and Dubinin–Radushkevich isotherms studies of equilibrium sorption of $Zn^{2+}$ unto phosphoric acid modified rice husk, *IOSR J. Appl. Chem.*, 2012, **3**, 38–45.

38 S. Han, K. Liu, L. Hu, F. Teng, P. Yu and Y. Zhu, Superior adsorption and regenerable dye adsorbent based on flower-like molybdenum disulfide nanostructure, *Sci. Rep.*, 2017, **7**, 1–11.

39 Z. Geng, Y. Lin, X. Yu, Q. Shen, L. Ma, Z. Li, N. Pan and X. Wang, Highly efficient dye adsorption and removal: a functional hybrid of reduced graphene oxide–$Fe_3O_4$ nanoparticles as an easily regenerative adsorbent, *J. Mater. Chem.*, 2012, **22**, 3527–3535.

40 Y. Li, Q. Du, T. Liu, X. Peng, J. Wang, J. Sun, Y. Wang, S. Wu, Z. Wang and Y. Xia, Comparative study of methylene blue dye adsorption onto activated carbon, graphene oxide, and carbon nanotubes, *Chem. Eng. Res. Des.*, 2013, **91**, 361–368.

41 K. Babitha, J. J. Matilda, A. P. Mohamed and S. Ananthakumar, Catalytically engineered reduced graphene oxide/ZnO hybrid nanocomposites for the adsorption, photoactivity and selective oil pick-up from aqueous media, *RSC Adv.*, 2015, **5**, 50223–50233.

42 W. Fan, W. Gao, C. Zhang, W. W. Tjiu, J. Pan and T. Liu, Hybridization of graphene sheets and carbon-coated $Fe_3O_4$ nanoparticles as a synergistic adsorbent of organic dyes, *J. Mater. Chem.*, 2012, **22**, 25108–25115.